RSC Advances

PAPER

View Article Online
View Journal | View Issue

Cite this: *RSC Adv.*, 2017, **7**, 4555

In_4SnS_8 ultrathin nanosheets: a ternary sulfide with fast adsorption–visible-light photocatalysis dual function†

Shuling Shen,* Long Li, Zhujun Wu, Minquan Sun, Zhihong Tang and Junhe Yang*

Received 24th November 2016
Accepted 29th December 2016

DOI: 10.1039/c6ra27262b

www.rsc.org/advances

Ultrathin In_4SnS_8 nanosheets have been successfully synthesized *via* a facile thermal decomposition method. The average thickness of these In_4SnS_8 nanosheets is only 3.8 nm, comprising about five atomically thick layers. To our knowledge, this is the thinnest In_4SnS_8 nanosheet synthesized using a solution-phase chemical method. The resulting ultrathin In_4SnS_8 nanosheets exhibit fast adsorption–visible-light photocatalysis dual function for various organic dyes, suggesting their potential application in environmental remediation, solar energy conversion, and advanced optical/electric nanodevices.

Introduction

The advances in graphene technology have stimulated the synthesis and characterization of various two dimensional nanomaterials such as transition metal oxides,[1] metal chalcogenides,[2] and organic compounds,[3–5] in the field of nanotechnology. To obtain these 2D nanomaterials, tremendous efforts have been made and various physical and chemical synthesis methods have been developed, such as mechanical and liquid-phase exfoliations,[6–8] ion-intercalation[9,10] and exfoliation,[11–15] chemical vapor deposition (CVD),[16–18] and solution-phase chemical syntheses,[19] *etc.* However, simple, effective synthetic methods and well-defined 2D nanostructures are still being pursued.

Metal sulfides, as a typical class of semiconductor, have attracted much attention due to their extraordinary chemical/physical properties and multiple potential applications. In particular, ternary or quaternary metal sulfides (TQMS) have been extensively studied because of their unique optoelectronic and catalytic properties, as well as their other advantages such as low cost, earth-abundance, and low toxicity. These benefits offer TQMS increased opportunities in meeting the requirements of some special applications. For example, $ZnIn_2S_4$ with a band gap of 2.3 eV (ref. 20 and 21) and $Zn_xCd_{1-x}S$ with a tunable band gap within the visible light region[22,23] have been applied in visible-light photocatalysis. $CuInS_2$ (ref. 24) and Cu_2ZnSnS_4 (ref. 25 and 26) with band gaps of 1.5 eV have been used in low-cost photovoltaic devices. $CuInS_2$–ZnS with low toxicity and broad emission bands[27] has been used in light emitting devices. Compared with 0D quantum dots, 2D ultrathin TQMS nanosheets exhibit improved conductivity, flexibility, and high surface area, which are key elements for some applications. However, although the synthesis of TQMS nanocrystals has been widely reported recently, the controlled and convenient synthesis of TQMS with ultrathin 2D structures still remains a great challenge.

Here, we prepared 2D ultrathin In_4SnS_8 nanosheets *via* a facile thermal decomposition method. The ultrathin In_4SnS_8 nanosheets show fast adsorption–visible-light photocatalysis dual function for various organic dyes.

Experimental section

Chemicals

Indium trichloride ($InCl_3 \cdot 4H_2O$, 99.995%), tin(IV)chloride dihydrate ($SnCl_4 \cdot 5H_2O$, 98%), sodium diethyldithiocarbamate ($(C_2H_5)_2NCS_2Na \cdot 3H_2O$, Na(DDTC)), oleylamine (OM, 80–90%), octadecylene (ODE, ≥95.0%) absolute ethanol (AR), cyclohexane (99.5%), and acetic acid (AR) were all purchased from Sinopharm Chemical Reagent Company. All the chemicals were used as received without further purification.

Synthesis of $In(DDTC)_3$ and $Sn(DDTC)_4$

For synthesizing $In(DDTC)_3$, 10 mmol of $InCl_3 \cdot 4H_2O$ was dissolved in 100 mL of distilled water. Then 100 mL aqueous solution containing 30 mmol of $Na(DDTC) \cdot 3H_2O$ was dropped into the $InCl_3$ aqueous solution and the mixture was magnetically stirred for 1 h. The resulting white solution was then allowed to stand under ambient conditions. After 3 h, the resulting white precipitate was filtered, washed with distilled water and dried in an oven at 60 °C. $Sn(DDTC)_4$ was also prepared using the same method as that depicted above, with $InCl_3 \cdot 4H_2O$ replaced by $SnCl_4 \cdot 5H_2O$.

School of Materials Science and Engineering, University of Shanghai for Science and Technology, Shanghai, 200093, P. R. China. E-mail: slshen@usst.edu.cn; jhyang@usst.edu.cn

† Electronic supplementary information (ESI) available. See DOI: 10.1039/c6ra27262b

Synthesis of In_4SnS_8 nanosheets

In_4SnS_8 nanosheets were synthesized *via* a thermal decomposition method.[28] In a typical procedure, 0.1 mmol of $Sn(DDTC)_4$ and 0.4 mmol of $In(DDTC)_3$ were added into 20 mmol of OM solvent in a three-necked flask (100 mL). The slurry was heated to 120 °C under vacuum with vigorous magnetic stirring. Afterward, the slurry was heated to 240 °C at a rate of 15 °C min^{-1} and was then maintained at this temperature for 1 h under N_2 atmosphere. Then the reaction system was cooled down to room temperature naturally. The resultant mixture was centrifugally separated, and then the precipitates were washed with ethanol twice. The products were collected and stored in cyclohexane.

Because the adsorption and photocatalysis experiments were all carried out in aqueous solution, the obtained In_4SnS_8 nanosheets were treated in acetic acid to remove the stabilizing surfactant OM on the surface of the In_4SnS_8 nanosheets. Typically, the obtained samples were immersed in acetic acid at 70 °C for 10 h. The resulting photocatalysts were collected by centrifugation, washed with ethanol, and then dried at room temperature in the dark.

Removal of organic dyes

Adsorption performance of In_4SnS_8 nanosheets. 20 mg photocatalyst powder was dispersed in 100 mL aqueous solution containing 10 ppm of dye at room temperature (25 ± 2 °C). The suspension was placed in the dark under magnetic stirring at a speed of 300 rpm. At a given interval, a 5 mL aliquot of the suspension was taken and centrifuged. The adsorption of dye was monitored by measuring the absorption band of the dye on a UV-visible spectrophotometer. The adsorption rate was evaluated according to C/C_0 (C_0 is the initial density of dye; C is the density of dye after adsorption).

Photocatalytic degradation of dyes. Photocatalytic tests were carried out in an aqueous solution at ambient temperature. The light source was a 300 W Xe lamp with a UV cut off filter ($\lambda > 420$ nm) to allow only visible light to transmit. Briefly, 20 mg photocatalyst powder was dispersed in a 100 mL aqueous solution containing 10 ppm of dye. The solution was placed in the dark to reach adsorption–desorption equilibrium. After that, the suspension was irradiated under visible light from the above glass reactor at a distance of 10 cm. The temperature of the reaction system was kept at room temperature by using a water cooling system. At a given irradiation time interval, 5 mL of the suspension was collected and centrifuged to separate the photocatalyst. Photodegradation was monitored by measuring the absorption band of the dye on a UV-visible spectrophotometer. The degradation rate was evaluated according to C/C_0 (C_0 is the density of dye after adsorption equilibrium; C is the density of dye after reaction). To evaluate the stability of the photocatalyst, after the photochemical reaction, the photocatalyst was separated from the suspension, washed with water, and dried at 60 °C in the dark, and then the recovered photocatalyst was used for the next run of the photoreaction under the same conditions.

Characterization. The morphology and size of the obtained sample were examined on a Tecnai G2 F30 S-Twin transmission electron microscope (TEM, FEI, USA) operated at 200 kV. Powder X-ray diffraction (XRD) patterns were recorded on a Bruker D8 Advance powder X-ray diffractometer at a scanning rate of 4° min^{-1}, with Cu Kα radiation (λ = 1.5406 Å) in the range of 20–70°. X-ray photoelectron spectra (XPS) were recorded using a PHI 5000 Versaprobe spectrometer fitted with a monochromated Al Kα X-ray source ($h\nu$ = 1486.6 eV). The XPS binding energies were calibrated by referencing the C 1s to 284.6 eV. UV-vis absorption spectra were obtained on a Lambda 25 UV-vis-NIR spectrometer (PerkinElmer, USA), and photoluminescence (PL) spectra were collected on a fluorescence spectrometer (HITACHI, F-4600) at room temperature.

Results and discussion

Fig. 1a–c depicts the morphology of the In_4SnS_8 nanosheets. Large film structures of tens of micrometres in size are obtained (Fig. 1a), and clear basic features of the film are nanosheets with wrinkles (white arrows) and rags (red arrows). In the TEM image, the wrinkles induced by the surface tension of the nanosheets are more obvious, due to the ultrathin nature of the nanosheets, which is quite similar to graphene (Fig. 1b and c).

The XRD pattern in Fig. 1d indicates that no other impurities such as SnS or In_2S_3 are detected in the sample. The peaks at 28.2°, 33.1°, 48.1°, 50.1° and 58.6° can be indexed to the (6 0 0), (6 0 2), (1 7 4), (0 0 1) and (4 4 6) planes of the tetragonal phase of In_4SnS_8, respectively, in agreement with the literature reports.[29] The lattice spacing of 0.31 nm in the HRTEM image can be indexed as the (600) plane of tetragonal In_4SnS_8, indicating the confined growth of the In_4SnS_8 nanosheets along the ⟨100⟩ direction. In addition, the energy-dispersive X-ray spectroscopy (EDS) data (Fig. S1†) further verify the formation of the In_4SnS_8 compound (In : Sn : S atomic ratio = 3.95 : 1 : 8.07).

An AFM image was recorded to acquire more information on the nanosheets. Fig. 2a shows the representative AFM image of the edges of the In_4SnS_8 nanosheets. The average thickness is determined to be about 3.8 nm according to the height difference at the sites of H1 and H2. The theoretical thickness of an In_4SnS_8 monolayer is 0.697 nm (Fig. 2c), suggesting the obtained In_4SnS_8 nanosheets comprise about five atomically thick layers. To our knowledge, these are the thinnest In_4SnS_8 nanosheets synthesized *via* a solution-phase chemical method.

To gain insight into the composition of the nanosheets and the elemental oxidation states present, XPS was performed and the results are shown in Fig. 3. The survey XPS spectrum in Fig. 3a indicates the presence of In, Sn and S components as well as C, O and N impurities. C (C 1s, 284.6 eV), O (O 1s, 531.8 eV) and N (N 1s, 399.6 eV) in the product may be due to absorbed organic ligands of solvent and gaseous molecules. Fig. 3b reveals that the binding energies of 444.7 eV and 452.3 eV correspond to In $3d_{5/2}$ and In $3d_{3/2}$, respectively, suggesting the presence of In^{3+} in the sample. Fig. 3c shows that there are two strong peaks at 485.8 eV and 494.2 eV, which can be assigned to Sn $3d_{5/2}$ and Sn $3d_{3/2}$, respectively, confirming the Sn^{4+} oxidation state of the Sn element in the sample. The S

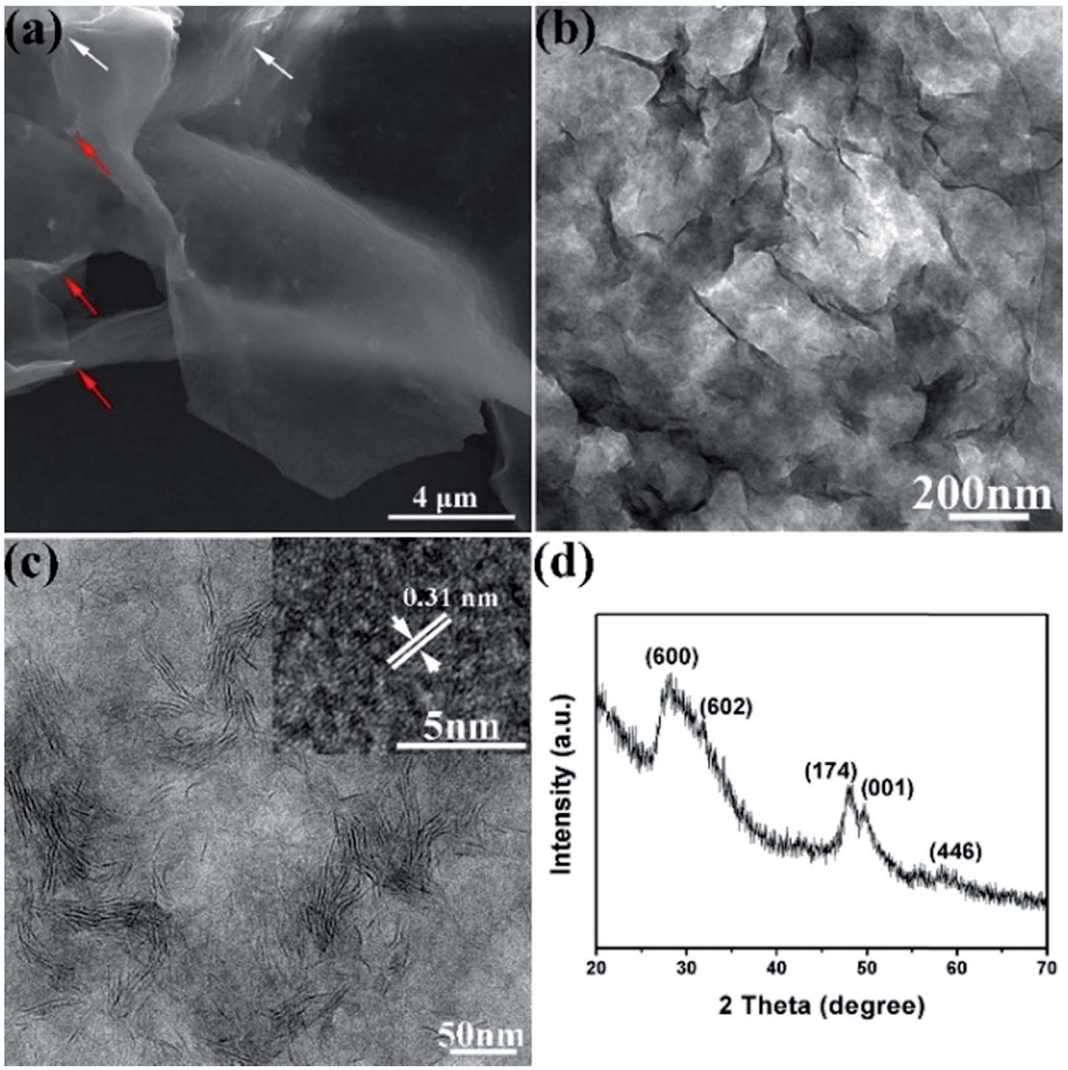

Fig. 1 SEM (a) and TEM (b and c) images and XRD pattern (d) of the In_4SnS_8 nanosheets. The inset in (c) is the HRTEM image of the In_4SnS_8 nanosheets.

2p peak splits into two peaks, and these are located at 161.0 eV and 162.6 eV, indicating that S exists in sulfide phases.

Composition analysis was conducted at the nanoscale to further prove the formation of ternary sulphide In_4SnS_8. The EDS elemental mapping images (Fig. 4) directly indicate that In, Sn and S are homogeneously distributed in the nanosheets, which excludes the existence of compositional gradients within the nanosheets or multiphase coexistence. Consequently, the as-synthesized products can be determined to be pure ultrathin In_4SnS_8 nanosheets, based on the results of TEM, AFM, XRD, EDS, EDS element mapping and XPS measurements.

It is found that OM plays an important role in the formation of the In_4SnS_8 ultrathin nanosheets. In our previous research, we found that OM plays two roles during the formation of low dimensional metal sulfide nanocrystals synthesized using a single-source precursor method: (1) as a catalyst to accelerate the decomposition of single source precursors; (2) as a stabilizer for the growth of low dimensional nanocrystals.[19,28] As shown in Fig. S2,† when only ODE is used as the solvent, only $Sn(DDTC)_4$ decomposes and $In(DDTC)_3$ does not decompose (Fig. S2†). When a certain amount of OM is mixed with ODE as the solvent, both $Sn(DDTC)_4$ and $In(DDTC)_3$ decompose and In_4SnS_8 is obtained (Fig. S1†). However, although In_4SnS_8 can be formed in the mixture of ODE and OM, the sample does not consist of pure nanosheets, but a mixture of nanoparticles and nanosheets (Fig. S3†). This means that OM can control the nucleation and growth kinetics of In_4SnS_8 nanocrystals. According to above results, the mechanism for the formation of the In_4SnS_8 nanosheets is proposed as shown in Scheme 1: in the presence of sufficient OM, both $Sn(DDTC)_4$ and $In(DDTC)_3$ decompose and In_4SnS_8 nuclei form. OM molecules simultaneously selectively adsorb on the (600) plane of newly generated In_4SnS_8 nuclei, leading to the formation of two dimensional In_4SnS_8 nanosheets.

Fig. 5 shows the UV-vis absorption and PL spectra of the In_4SnS_8 nanosheets. This shows that the In_4SnS_8 nanosheets have an intense absorption and emission in the visible light

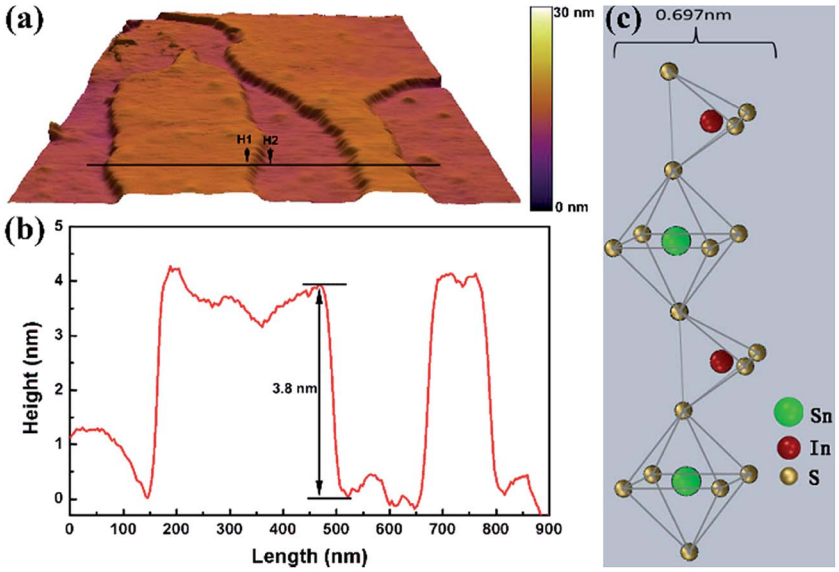

Fig. 2 (a) AFM image, (b) height profile along the line in AFM image, and (c) the theoretical thickness of In_4SnS_8 monolayer.

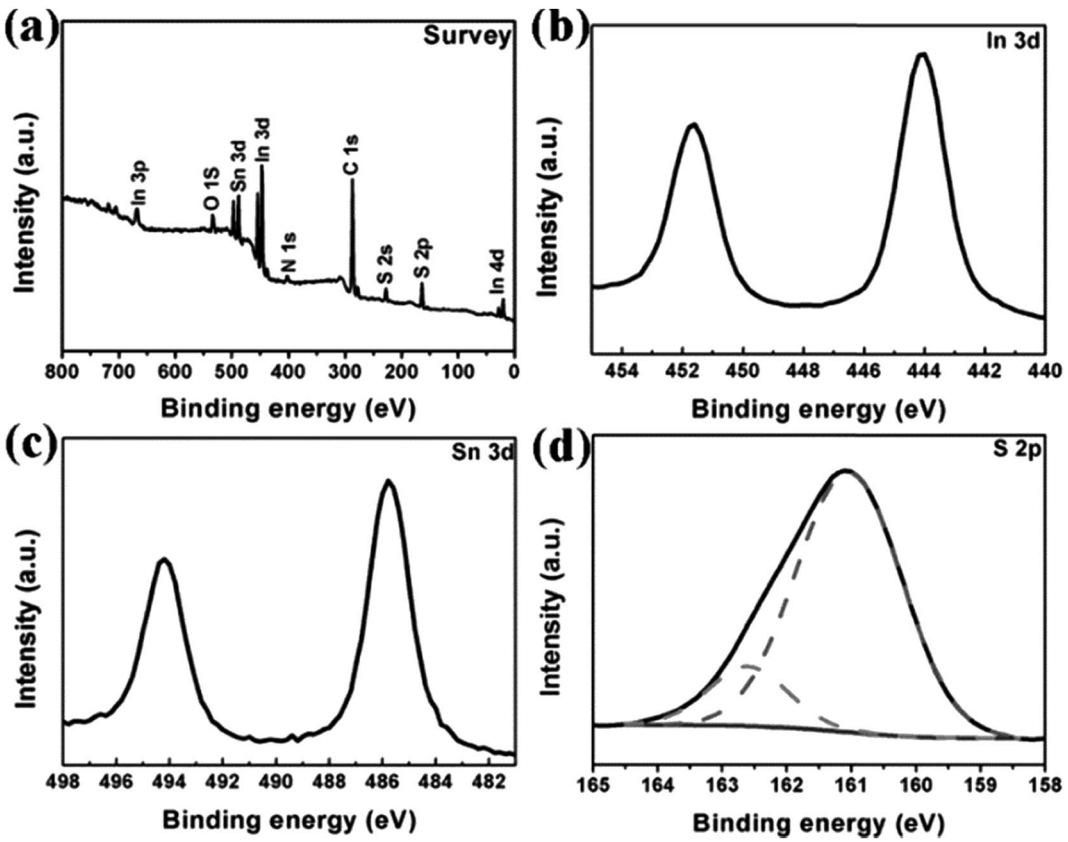

Fig. 3 XPS spectra of the In_4SnS_8 nanosheets: (a) typical survey spectrum of the In_4SnS_8 nanosheets and high-resolution core level spectra of (b) In 3d, (c) Sn 3d and (d) S 2p.

region. The intrinsic absorption edge of these In_4SnS_8 nanosheets shows an obvious blue shift with respect to the reported values for flower-like In_4SnS_8 microspheres,[30] suggesting the presence of a quantum confinement in the band structure due to the ultrathin thickness of the In_4SnS_8 nanosheets. In addition, Wang *et al.*[30] reported that the flower-like In_4SnS_8 microspheres with specific surface areas of 24.7 $m^2\ g^{-1}$ exhibited excellent removal efficiency of Cr(VI). The specific surface area of our In_4SnS_8 nanosheets is 40.34 $m^2\ g^{-1}$, which is much higher than that of flower-like In_4SnS_8 microspheres. The

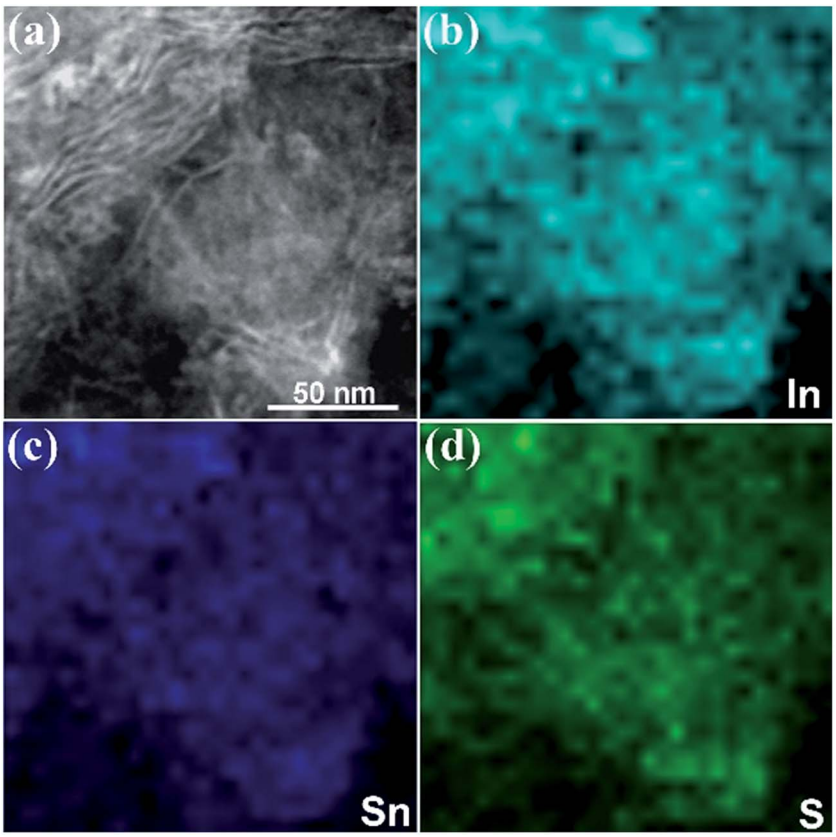

Fig. 4 (a) STEM image of the In_4SnS_8 nanosheets, and (b–d) the corresponding In, Sn and S element mapping images.

ultrathin 2D structure, large surface area and visible-light response of the In_4SnS_8 nanosheets make them suitable for photocatalytic applications.

In the photocatalytic degradation test, before irradiation using light, the dye solution containing photocatalyst powder was stirred in the dark to reach absorption equilibrium. It was found that for some dyes, such as methylene blue, congo red, azure II, amido black 10B, and rhodamine B, the adsorption maxima are reached within only 10 min (Fig. 6a). The adsorption rates are all larger than 95%. For congo red, the adsorption rate in 10 min is as high as 99.1%. Simultaneously, it was also observed that for some of the other dyes such as indigotine and orange G (OG), the adsorption maxima are reached in an even longer time of 40 min, with adsorption rates of only 45% and 30%, respectively. The difference in adsorption capacity of the In_4SnS_8 nanosheets for the dyes can be attributed to the molecular weights of the dyes (Table 1). With a decrease in the molecular weight of the dye, the adsorption rate decreases. This is because the adsorption of nonpolar dyes on the In_4SnS_8 nanosheets mainly belongs to physical adsorption, which is determined by dispersion force.[31] When the molecular weight is larger, the dispersion force is stronger and the absorption rate is higher. Methylene blue and rhodamine B are polar molecules. The adsorption of these molecules on the In_4SnS_8 nanosheets is a chemical adsorption. So, although their molecular weights are small, the adsorption rates are as high as that of the dyes with large molecular weights.

It can be seen from Fig. 6a and Table 1 that the adsorption rate of OG with a small molecular weight is only 30% after 40 min and after this time it reaches absorption equilibrium. In order to completely remove OG, a photocatalytic reaction can be employed by utilizing the visible-light response properties of the In_4SnS_8 nanosheets. It can be seen from Fig. 6b that after 30 min of visible light irradiation, nearly 92% of OG is degraded, showing the excellent photocatalytic activity of the as-prepared In_4SnS_8 nanosheets. For comparison, commercial P25 was used as a photocatalyst and the photocatalytic reaction was carried out under the same conditions. The commercial P25 exhibits almost no adsorption for OG and the photodegradation rate of OG over P25 is close to zero under visible-light irradiation. In addition, the photodegradation rates of OG on the In_4SnS_8 nanosheets irradiated under a Xe lamp with a UV cut off filter (visible light) and without a UV cut off filter (UV light and visible light), were also compared. The result shown in Fig. S5† indicates that the photodegradation rate of OG on the In_4SnS_8 nanosheets without the UV cut off filter is only slightly higher than that of OG on the In_4SnS_8 nanosheets with the UV cut off filter. This means that the ultrathin In_4SnS_8 nanosheets mainly respond to visible light. The above results indicate that the ultrathin In_4SnS_8 nanosheets preserve fast adsorption and visible-light photocatalysis dual function for the complete removal of various organic dyes.

The stability of photocatalysts is an important factor for their practical application. Therefore, the In_4SnS_8 nanosheets were

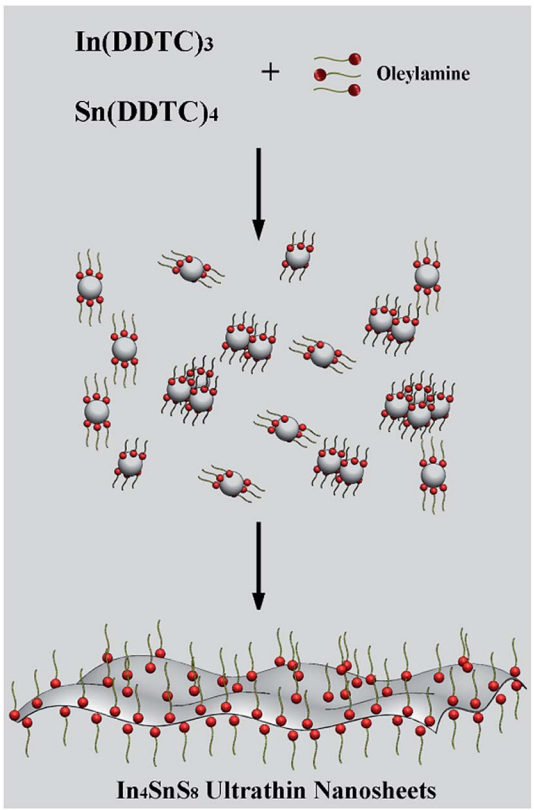

Scheme 1 Schematic illustration of the formation mechanism of ultrathin In_4SnS_8 nanosheets.

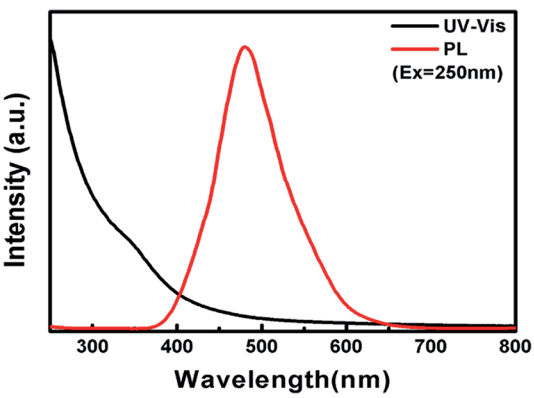

Fig. 5 UV-vis absorption (black line) and PL (red line) spectra of the In_4SnS_8 nanosheets.

recycled four times under visible light irradiation to examine their stability. After each reaction, the photocatalyst was collected and washed using deionized water and separated by centrifugation from the aqueous suspension. Afterward, the photocatalysts were dried in a vacuum at 40 °C for 10 h and used for the next recycling reaction. Fig. 6c shows that the photodegradation rate can still be maintained above 85% after four cycles. The TEM image in Fig. S4† of the In_4SnS_8 nanosheets after recycling indicates that after four cycles, the In_4SnS_8 nanosheets maintain their film like structure, but are more

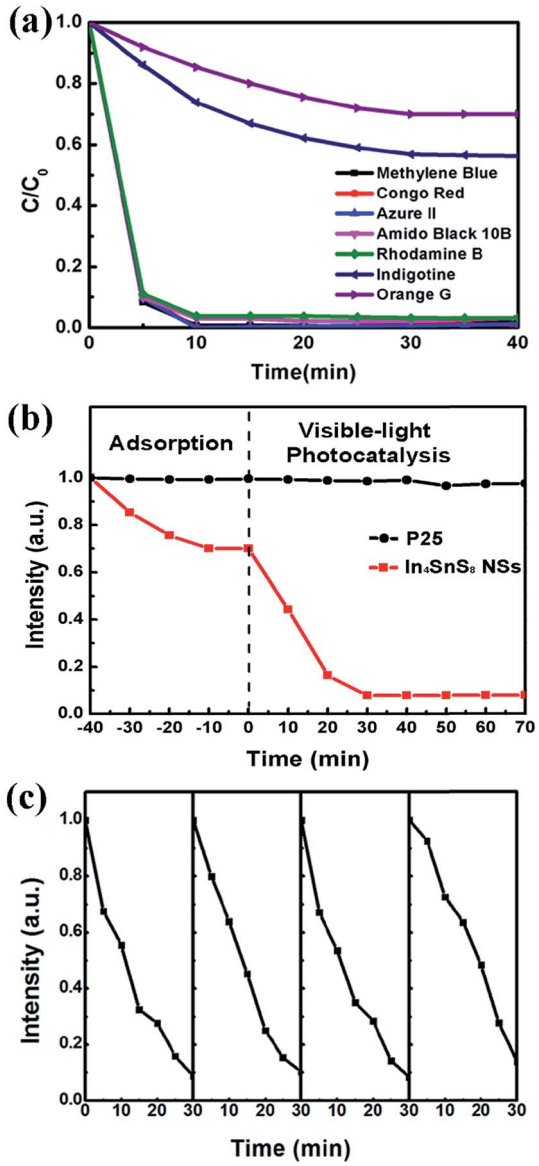

Fig. 6 (a) The adsorption of various dyes on the In_4SnS_8 nanosheets. (b) Adsorption and visible-light photodegradation rate of OG on the In_4SnS_8 nanosheets and P25. (c) Typical time course of the photocatalytic degradation of OG over the In_4SnS_8 nanosheets under visible light.

Table 1 Molecular weights and adsorption rates of various dyes

Dyes	Molecular weight	Adsorption rate
Congo red	696.68	99.1%
Azure II	625.68	98.8%
Amido black 10B	616.49	97%
Rhodamine B	479	96.8%
Methylene blue	320	98.4%
Indigotine	466.37	45%
Orange G	452.37	30%

aggregated compared with the as-prepared nanosheets. This may be due to the repeated washing and drying during the recycling reaction. HRTEM and XRD measurements indicate that the crystal structure of In_4SnS_8 remains unchanged after the recycling test, suggesting the high stability of the In_4SnS_8 nanosheets.

Based on the above discussion, the mechanism for dye removal from water using the In_4SnS_8 nanosheets mainly involves two steps: (1) the nonpolar dye molecules are adsorbed on the surface of the ultrathin In_4SnS_8 nanosheets by dispersion force. (2) Under the irradiation of visible light, the electrons in the valence band (VB) of the In_4SnS_8 nanosheets are excited to the conduction band (CB). The CB band of In_4SnS_8 (−0.76 eV (ref. 30)) is more negative than the standard redox potential of (O_2/$^{\bullet}O_2^-$) (−0.33 eV *vs.* NHE),[32] suggesting that electrons at the CB of In_4SnS_8 can reduce O_2 to $^{\bullet}O_2^-$. With the help of the superoxide radical, the dye molecules can be translated into CO_2 and H_2O, *etc.* The VB potential of In_4SnS_8 (1.51 eV (ref. 30)) is more negative than the standard redox potential of (OH^-/$^{\bullet}OH$) (1.99 eV *vs.* NHE),[33] suggesting that the generated holes in In_4SnS_8 cannot oxidize OH^- or H_2O to the hydroxy radical $^{\bullet}OH$. To further confirm the absence of the hydroxy radical, a fluorescence method was adopted using terephthalic acid (TA) as a probe molecule.[34,35] TA can react with the hydroxy radical to produce the highly fluorescent product, 2-hydroxyterephthalic acid (TAOH), which has a maximum emission intensity in its fluorescence spectra at 425 nm by excitation at 315 nm. However, the result in Fig. S6† indicates that the characteristic peak of TAOH at 425 nm was not detected during the whole irradiation time, meaning no hydroxy radicals were produced under visible light irradiation in the presence of the In_4SnS_8 nanosheet photocatalyst, which is consistent with the theoretical analysis (Scheme 2).

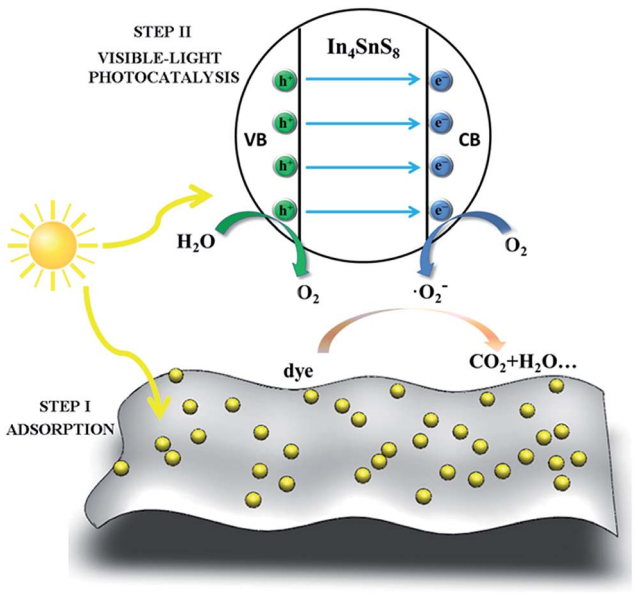

Scheme 2 Schematic diagram of the removal of dyes by the ultrathin In_4SnS_8 nanosheets through adsorption and visible-light photodegradation.

Conclusions

In_4SnS_8 ultrathin nanosheets were synthesized *via* a facile thermal decomposition process. SEM, TEM and EDS element mapping results indicated the 2D nature of the In_4SnS_8 nanosheets. The AFM results indicated that the thickness of the In_4SnS_8 nanosheets was only 3.8 nm, consisting of about five atomically thick layers. The In_4SnS_8 ultrathin nanosheets exhibited fast and high adsorption capacities for various organic dyes. For nonpolar dyes, the adsorption rates were related to their molecular weights. Nonpolar dyes of small molecular weights and low adsorption rates, such as OG, could be degraded up to 92% under visible light irradiation, using the In_4SnS_8 nanosheets as a photocatalyst. The as-obtained In_4SnS_8 ultrathin nanosheets may have potential applications in environmental remediation and solar energy conversion.

Acknowledgements

The authors gratefully acknowledge the financial support of NSFC (21101166, 51272157, and 51472160), Key Basic Research Program of Shanghai Municipal Science and Technology Commission (13NM1401102), Innovation Program of Shanghai Municipal Education Commission (14YZ084), and the Hujiang Foundation of China (B14006).

Notes and references

1 G. Xiang, T. Li, J. Zhuang and X. Wang, *Chem. Commun.*, 2010, **46**, 6801–6803.
2 Y. Zhang, J. Lu, S. Shen, H. Xu and Q. Wang, *Chem. Commun.*, 2011, **47**, 5226–5228.
3 A. Kudo and Y. Miseki, *Chem. Soc. Rev.*, 2009, **38**, 253–278.
4 T. Rodenas, I. Luz, G. Prieto, B. Seoane, H. Miro, A. Corma, F. Kapteijn, F. X. L. Xamena and J. Gascon, *Nat. Mater.*, 2015, **14**, 48–55.
5 C. Tan, X. Qi, X. Huang, J. Yang, B. Zheng, Z. An, R. Chen, J. Wei, B. Z. Tang, W. Huang and H. Zhang, *Adv. Mater.*, 2014, **26**, 1735–1739.
6 J. Lauth, F. E. S. Gorris, M. SamadiKhoshkhoo, T. Chassé, W. Friedrich, V. Lebedeva, A. Meyer, C. Klinke, A. Kornowski, M. Scheele and H. Weller, *Chem. Mater.*, 2016, **28**, 1728–1736.
7 J. S. Son, X. D. Wen, J. Joo, J. Chae, S. I. Baek, K. Park, J. H. Kim, K. An, J. H. Yu, S. G. Kwon, S. H. Choi, Z. Wang, Y. W. Kim, Y. Kuk, R. Hoffmann and T. Hyeon, *Angew. Chem., Int. Ed.*, 2009, **48**, 6861–6864.
8 D. Yoo, M. Kim, S. Jeong, J. Han and J. Cheon, *J. Am. Chem. Soc.*, 2014, **136**, 14670–14673.
9 Y. Liu, J. Xiong, S. Luo, R. Liang, N. Qin, S. Liang and L. Wu, *Chem. Commun.*, 2015, **51**, 15125–15128.
10 Z. Zeng, T. Sun, J. Zhu, X. Huang, Z. Yin, G. Lu, Z. Fan, Q. Yan, H. H. Hng and H. Zhang, *Angew. Chem., Int. Ed.*, 2012, **51**, 9052–9056.
11 J. R. Brent, N. Savjani, E. A. Lewis, S. J. Haigh, D. J. Lewis and P. O'Brien, *Chem. Commun.*, 2014, **50**, 13338–13341.

12 U. Khan, P. May, A. O'Neill, A. P. Bell, E. Boussac, A. Martin, J. Semple and J. N. Coleman, *Nanoscale*, 2013, **5**, 581–587.
13 H. Li, G. Lu, Y. Wang, Z. Yin, C. Cong, Q. He, L. Wang, F. Ding, T. Yu and H. Zhang, *Small*, 2013, **9**, 1974–1981.
14 K. Varoon, X. Zhang, B. Elyassi, D. D. Brewer, M. Gettel, S. Kumar, J. A. Lee, S. Maheshwari, A. Mittal, C. Y. Sung, M. Cococcioni, L. F. Francis, A. V. McCormick, K. A. Mkhoyan and M. Tsapatsis, *Science*, 2011, **334**, 72–75.
15 J. Zheng, H. Zhang, S. Dong, Y. Liu, C. T. Nai, H. S. Shin, H. Y. Jeong, B. Liu and K. P. Loh, *Nat. Commun.*, 2014, **5**, 2995.
16 Y. H. Lee, X. Q. Zhang, W. Zhang, M. T. Chang, C. T. Lin, K. D. Chang, Y. C. Yu, J. T. Wang, C. S. Chang, L. J. Li and T. W. Lin, *Adv. Mater.*, 2012, **24**, 2320–2325.
17 J. C. Shaw, H. Zhou, Y. Chen, N. O. Weiss, Y. Liu, Y. Huang and X. Duan, *Nano Res.*, 2015, **7**, 511–517.
18 J. Yuan, J. Wu, W. J. Hardy, P. Loya, M. Lou, Y. Yang, S. Najmaei, M. Jiang, F. Qin, K. Keyshar, H. Ji, W. Gao, J. Bao, J. Kono, D. Natelson, P. M. Ajayan and J. Lou, *Adv. Mater.*, 2015, **27**, 5605–5609.
19 S. Shen, Y. Zhang, L. Peng, Y. Du and Q. Wang, *Angew. Chem., Int. Ed.*, 2011, **50**, 7115–7118.
20 B. Chai, T. Peng, P. Zeng, X. Zhang and X. Liu, *J. Phys. Chem. C*, 2011, **115**, 6149–6155.
21 J. Hou, C. Yang, H. Cheng, Z. Wang, S. Jiao and H. Zhu, *Phys. Chem. Chem. Phys.*, 2013, **15**, 15660–15668.
22 A. Ma, Z. Tang, S. Shen, L. Zhi and J. Yang, *RSC Adv.*, 2015, **5**, 27829–27836.
23 S. Shen, A. Ma, Z. Tang, Z. Han, M. Wang, Z. Wang, L. Zhi and J. Yang, *ChemCatChem*, 2015, **7**, 609–615.
24 B. D. Weil, S. T. Connor and Y. Cui, *J. Am. Chem. Soc.*, 2010, **132**, 6642–6643.
25 Q. Guo, H. W. Hillhouse and R. Agrawal, *J. Am. Chem. Soc.*, 2009, **131**, 11672–11673.
26 C. Steinhagen, M. G. Panthani, V. Akhavan, B. Goodfellow, B. Koo and B. A. Korgel, *J. Am. Chem. Soc.*, 2009, **131**, 12554–12555.
27 H. Kim, J. Y. Han, D. S. Kang, S. W. Kim, D. S. Jang, M. Suh, A. Kirakosyan and D. Y. Jeon, *J. Cryst. Growth*, 2011, **326**, 90–93.
28 S. Shen, Y. Zhang, Y. Liu, L. Peng, X. Chen and Q. Wang, *Chem. Mater.*, 2012, **24**, 2407–2413.
29 Y. Lei, G. Wang, L. Zhou, W. Hu, S. Song, W. Fan and H. Zhang, *Dalton Trans.*, 2010, **39**, 7021–7024.
30 L. Wang, X. Li, W. Teng, Q. Zhao, Y. Shi, R. Yue and Y. Chen, *J. Hazard. Mater.*, 2013, **244–245**, 681–688.
31 J. Shi, J. Zheng, P. Wu and X. Ji, *Catal. Commun.*, 2008, **9**, 1846–1850.
32 Z. Li, Z. Xie, Y. Zhang, L. Wu, X. Wang and X. Fu, *J. Phys. Chem. C*, 2007, **111**, 18348–18352.
33 W. Liu, M. Wang, C. Xu, S. Chen and X. Fu, *Mater. Res. Bull.*, 2013, **48**, 106–113.
34 R. Bera, S. Kundu and A. Patra, *ACS Appl. Mater. Interfaces*, 2015, **7**, 13251–13259.
35 K. Ishibashi, A. Fujishima, T. Watanabe and K. Hashimoto, *Electrochem. Commun.*, 2000, **2**, 207–210.